# Design and Fabrication of Ultralight High-Voltage Power Circuits for Flapping-Wing Robotic Insects

Michael Karpelson, *Student Member, IEEE,* John P. Whitney,
Gu-Yeon Wei, *Member, IEEE,* Robert J. Wood, *Member, IEEE*
School of Engineering and Applied Sciences, Harvard University
Contact e-mail: michaelk@seas.harvard.edu

***Abstract*— Flapping-wing robotic insects are small, highly maneuverable flying robots inspired by biological insects and useful for a wide range of tasks, including exploration, environmental monitoring, search and rescue, and surveillance. Recently, robotic insects driven by piezoelectric actuators have achieved the important goal of taking off with external power; however, fully autonomous operation requires an ultralight power supply capable of generating high-voltage drive signals from low-voltage energy sources. This paper describes high-voltage switching circuit topologies and control methods suitable for driving piezoelectric actuators in flapping-wing robotic insects and discusses the physical implementation of these topologies, including the fabrication of custom magnetic components by laser micromachining and other weight minimization techniques. The performance of laser micromachined magnetics and custom-wound commercial magnetics is compared through the experimental realization of a tapped inductor boost converter capable of stepping up a 3.7V Li-poly cell input to 200V. The potential of laser micromachined magnetics is further shown by implementing a similar converter weighing 20mg (not including control functionality) and capable of up to 70mW output at 200V and up to 100mW at 100V.**

## I. Introduction

Flapping-wing robotic insects are a class of micro air vehicles (MAVs) that take design cues from biological insects in order to achieve a small size, high maneuverability, and hovering ability. Such robotic platforms have a number of applications, including exploration, environmental monitoring, search and rescue, and surveillance. Recently, the 60mg Harvard Microrobotic Fly (HMF), shown in Fig. 1, became the first such device capable of lifting off with external power [1]. The development of a power electronics package that can meet the stringent weight and power requirements of hovering flight is a crucial step towards enabling operation without an external power source.

The wing flapping motion in the HMF is powered by piezoelectric actuators, which offer robust mechanical performance, high efficiency, and high power density at small scales, and are expected to outperform conventional actuators, such as DC motors, in insect-scale devices [2]. From the perspective of power electronic design, piezoelectric actuators present two challenges. Firstly, they require high voltages to operate; for example, the actuators used in the HMF are driven in the range of 200-300V. Secondly, only a fraction of the input electrical energy is converted to mechanical output, while the remainder is stored in the capacitive structure of the actuator and must be recovered to maximize system efficiency [3].

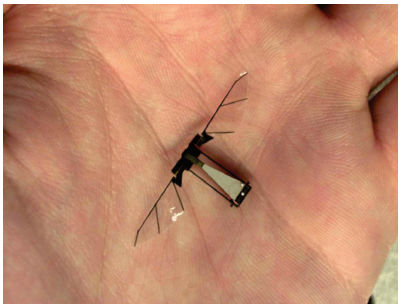

Fig. 1. Harvard Microrobotic Fly.

Most compact energy sources suitable for microrobotic applications, such as lithium batteries or fuel cells [4], generate output voltages below 5V. Connecting many unit cells in series to obtain high voltage is generally not practical because the packaging overhead causes a significant reduction in energy density. Consequently, the generation of high voltages for HMF actuators requires voltage conversion circuits with step-up ratios ranging from 50 to 100. While there are a number of circuit topologies with high step-up ratios, many of them cannot be easily miniaturized and/or suffer from poor efficiency at the output power levels common in microrobotic applications. Previous work described power circuit topologies and control algorithms that are amenable to miniaturization while achieving high system efficiency and power density [5].

This paper focuses on the physical implementation of lightweight, high-voltage power circuits suitable for driving piezoelectric and other capacitive actuators in microrobotic applications. Section II reviews the electrical properties of piezoelectric actuators and describes drive circuit topologies and control algorithms. Section III discusses techniques for minimizing the weight of high-voltage power circuits, including fabrication of custom magnetic components and circuit assembly methods. Section IV presents experimental results that apply these weight minimization techniques to one of the circuit topologies described in Section II. The performance of custom magnetic components is compared to the performance of magnetics manufactured using commercially available parts, and an ultralight implementation of a high step-up ratio DC-DC converter is presented.

978-1-4244-8085-2/11/$26.00 ©2011 IEEE

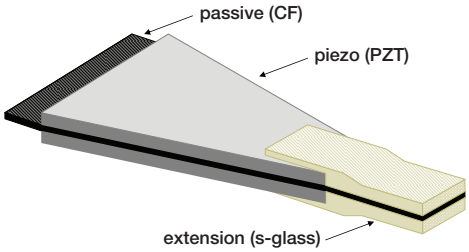


Fig. 2. Piezoelectric bimorph structure.

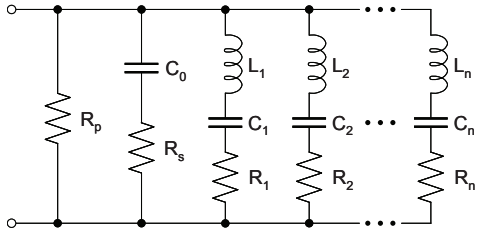


Fig. 3. Piezoelectric element equivalent circuit.

## II. Piezoelectric Drive Methods and Circuits

Piezoelectric actuators are available in many configurations, including linear devices such as stack actuators and bending devices such as unimorph and bimorph cantilevers. For example, the power actuator of the HMF uses a composite bimorph actuator optimized for energy density [6]. The actuator consists of two layers of PZT bonded to a central layer of carbon fiber, as well as an extension made of s-glass (Fig. 2). When a voltage is applied across one of the PZT layers, the layer contracts in the horizontal direction, causing the tip of the actuator to deflect vertically due to strain mismatch.

### A. Electrical model and drive methods

In the electrical domain, a piezoelectric element can be represented with an equivalent circuit where impedance is linked to the mechanical properties of the actuator and its load. This paper adopts the equivalent circuit of [7], shown in Fig. 3. The circuit can be divided into a static part, which represents the primary capacitance by $C_0$, dielectric losses by $R_p$, and hysteresis losses by $R_s$, and a number of resonant branches, each corresponding to a mechanical vibration mode. In each branch, $L_i$, $R_i$, and $C_i$ represent the equivalent mass, damping coefficient, and spring constant, respectively, of the vibration mode. Although hysteresis, as a nonlinear loss mechanism, cannot be fully represented by linear circuit components, the equivalent circuit parameters can be chosen to provide a good approximation of the hysteresis losses for a given drive voltage and operating frequency [3].

The equivalent circuit can adequately represent a dual-electrode piezoelectric actuator, such as a stack or unimorph bending actuator, or a single piezoelectric element in a multi-electrode actuator such as a bimorph. Table I shows some of the parameters for a typical bimorph bending actuator connected to the wings of the HMF, including the first two resonant modes.

TABLE I
Equivalent Circuit Parameters of Bimorph Actuator

| Static parameters | Value | Dynamic parameters | Mode 1 | Mode 2 |
|---|---|---|---|---|
| $C_0$ | 14.5nF | $L_i$ | 3.52kH | 1.03kH |
| $R_s$ | 100Ω | $C_i$ | 2nF | 0.8nF |
| $R_p$ | 10MΩ | $R_i$ | 130kΩ | 38kΩ |

Piezoelectric actuators may be driven with either a bipolar or a unipolar signal. In bipolar driving, the drive voltage varies between a positive or negative voltage, while in unipolar driving, the voltage is only positive. In microrobotic applications such as [1] or [8], piezoelectric actuators provide power for locomotion, which requires large strains and therefore high actuation voltages to enable large wing or leg strokes. Since high-amplitude bipolar drive signals can result in the depolarization of the piezoelectric element, the drive signal must be unipolar.

The equivalent circuit also shows that the majority of the energy stored in the actuator remains in the primary capacitance $C_0$ (in fact, the values of the capacitors $C_0$ and $C_1$ through $C_n$ are proportional to the amount of energy that, for a given operating voltage, can be stored in the primary capacitance and the vibration modes). As noted in [3], this energy is recoverable, and therefore the drive circuit should be capable of returning this energy to the supply or to a second piezoelectric layer that is activated 180° out of phase with the first. The second layer can belong to another actuator or the opposite half of a bimorph actuator.

Applying a drive signal to a unimorph or other dual-electrode piezoelectric actuator involves a single variable unipolar voltage source connected directly to the electrodes of the actuator, as shown in Fig. 4(a). Two methods of applying a drive signal to a bimorph are shown in Fig. 4(b) and (c). The method of Fig. 4(b), termed alternating drive, includes two variable unipolar sources connected to the outer electrodes and operated 180° out of phase, with a common ground on the central electrode. The method of Fig. 4(c), termed simultaneous drive, consists of a constant high-voltage bias applied across the actuator and a variable unipolar source connected to the central electrode. Alternating drive requires $2n$ variable voltage sources per $n$ bimorphs, while simultaneous drive offers the possibility of sharing the high-voltage bias among multiple actuators and therefore requires $n$ variable sources and one bias per $n$ bimorphs.

### B. Drive circuit topologies

From a circuit design perspective, the variable voltage sources can be implemented in two fundamental ways: a two-stage design, where the first stage steps up the low battery

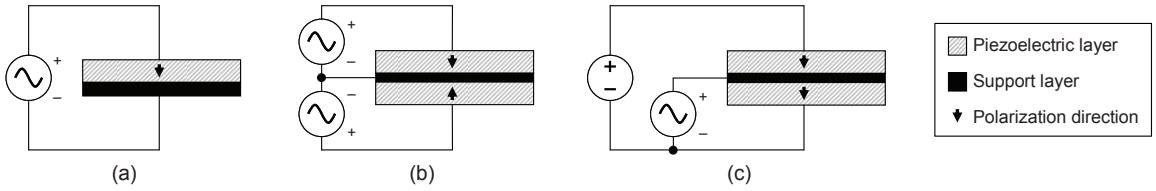


Fig. 4. Unipolar drive methods for piezoelectic actuators: unimorph (a), bimorph with alternating drive (b), and bimorph with simultaneous drive (c).

voltage to a high voltage and the second stage generates a time-varying drive signal; or a single-stage design, which simultaneously steps up the voltage and generates a time-varying signal. Since a two-stage design already generates a constant high-voltage output, it can easily be applied to the simultaneous drive method of Fig. 4(c), while a one-stage design is suitable for the alternating drive method of Fig. 4(b) and for dual-electrode actuators as in Fig. 4(a). Note that a two-stage design will generally have more components and larger weight, but will allow the sharing of the high-voltage bias. In contrast, a single-stage design will be more lightweight but cannot be shared. As a result, the selection of the drive method will depend on the number and type of actuators in a given system.

Fig. 5(a) shows a dual-stage drive circuit that can be used to drive a bimorph actuator in the simultaneous drive configuration of Fig. 4(c). The high-voltage bias is generated by a circuit configuration known as the tapped inductor boost converter, which consists of input capacitor $C_{in}$, switch $Q$, diode $D$, output capacitor $C_{hv}$, and tapped inductor $L_p/L_s$. A conventional pulse frequency modulation scheme (consisting of voltage reference $V_{ref}$, an analog comparator, a pulse generator, and a current sensor through $L_p$) produces a constant high voltage across output capacitor $C_{hv}$ for a range of load currents. Additional details on this topology can be found in [9] and [10].

To produce a time-varying drive signal from the output of the voltage conversion stage, switches $Q_L$ and $Q_H$ are used, along with diodes $D_H$ and $D_L$, and inductor $L$, forming a topology found in many switching amplifiers. Elements $C_{aH}$ and $C_{aL}$ represent the two layers of a piezoelectric bimorph. In low-power microrobotic applications, it is important to control this drive stage in a way that maximizes efficiency while generating the drive signal. The conventional approach to switching amplifiers uses the switch transistors to generate a PWM waveform, which is converted by an LC network into an output voltage equal to the average value of the PWM signal [11]. When connected to a primarily capacitive load with low energy dissipation, such an amplifier must actively charge and discharge the load during each switching cycle in order to maintain some voltage across the load [12]. This results in significant switching and conduction losses in the amplifier even when the output voltage is constant or changing slowly.

Here, an energy efficient control algorithm, proposed in [12], is used to generate unipolar high-voltage drive signals, 180° out of phase, across $C_{aH}$ and $C_{aL}$. An A/D converter monitors the voltage at the central terminal of the actuator. The value of the A/D conversion, along with the desired value of the voltage ($V_{ctrl}$), is used to address a memory table with pre-computed on-times for switches $Q_H$ and $Q_L$. The appropriate switch is then turned on for the prescribed length of time to either increase or reduce the voltage at the central terminal. A new A/D conversion begins after the current in $L$ returns to zero. This control algorithm results in a free-oscillating system that drives the voltage at the central terminal of the actuator towards the desired voltage $V_{ctrl}$. This results in a simple, efficient, and cost-effective system with low computational requirements.

To implement the drive methods of Fig. 4(a) and Fig. 4(b), which must simultaneously step up the input voltage and create a time-varying drive signal, the bidirectional flyback converter of Fig. 5(b) is used. Here, too, the modulation of switches $Q_H$ and $Q_L$ enables the charging and discharging of the piezoelectric layer, represented by $C_a$. Additional details on this topology can be found in [13]. Note that the control scheme for the drive stage of Fig. 5(a) can be applied here with no modifications except for the on-time values stored in the lookup table.

## III. Ultralight Circuit Fabrication

Insect-scale devices such as the HMF require extremely lightweight (milligram-scale) power circuits, which places significant constraints on all circuit components. In general, surface-mount capacitive and resistive components have low packaging overhead, and as a result it is difficult to reduce their weight further. Consequently, weight minimization efforts have been directed primarily at magnetics, semiconductor components, and the substrate.

### A. Magnetic components

Magnetic components are central to the implementation of the circuits in Fig. 5. Although there is a wide range of milligram-scale magnetic components available through commercial channels, very few are intended for high-voltage or high step-up ratio applications. For example, as of this writing, the smallest available flyback transformer with a sufficient turns ratio for use in the topologies of Fig. 5 (Coilcraft LPR4012 series) weighs 54mg, or almost the entire weight of the HMF. In previous work, magnetic components weighing 15-40mg had been implemented successfully using

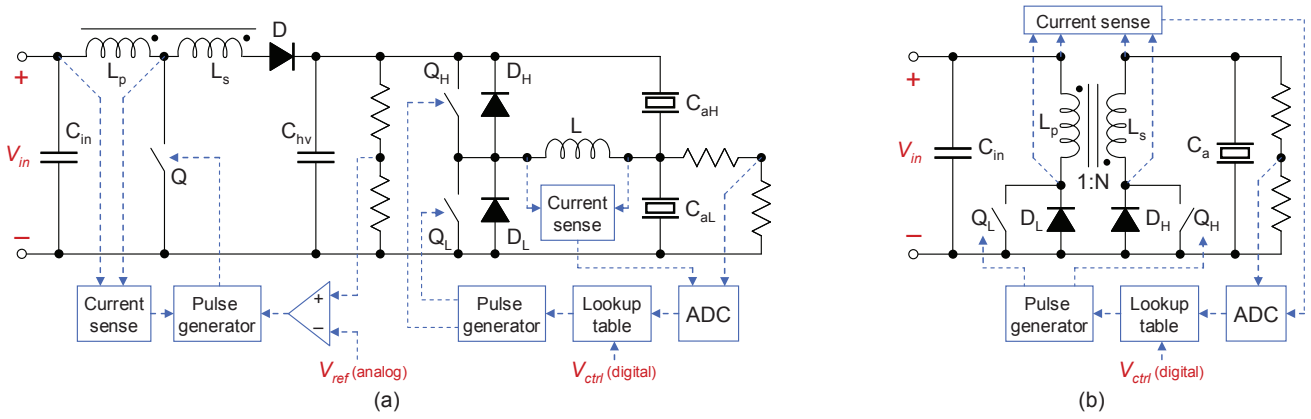


Fig. 5. Lightweight circuit topologies suitable for driving piezoelectric actuators. A tapped inductor boost converter combined with a switching amplifier drive stage (a) converts the input voltage to a constant high-voltage bias which is then used to produce a drive signal across piezoelectric layers $C_{aH}$ and $C_{aL}$, which represent a bimorph actuator. The bidirectional flyback converter (b) simultaneously steps up the voltage and generates a drive signal across piezoelectric layer $C_a$, representing a unimorph actuator or a single layer of a bimorph. In both cases, an A/D converter monitors the actuator voltage, which is then adjusted by modulating the switching transistors.

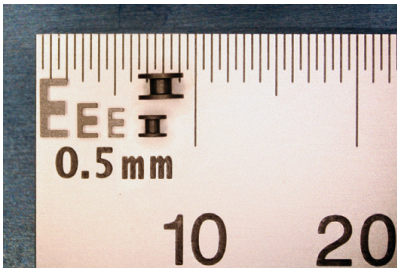


Fig. 6. E-cores fabricated by laser micromachining and bobbin cores salvaged from commercial inductors.

custom-wound ferrite bobbin cores salvaged from commercial inductors (e.g. the Coilcraft LPS3015 series) [5]. However, such implementations are limited to existing commercial core geometries. Furthermore, unshielded bobbin cores have poor electromagnetic interference (EMI) characteristics, which may have a detrimental effect on power electronics performance (as well as on the performance of other electronic systems) when several components are operating in close proximity, as would be expected in a microrobotic platform. Bobbin cores also make it more difficult to achieve good coupling between windings, particularly at higher winding ratios.

Laser ablation is a rapid and non-contact method of patterning [14] and cutting [15] ferrite materials, making it an attractive method for micromachining planar ferrite cores of arbitrary geometry. In particular, E-cores are a promising option for replacing the bobbin cores used in previous work, as they are simple to machine from planar sheets of ferrite, allow for precise control of inductance, and enable good magnetic coupling between windings. Although E-cores are not fully self-shielding, they also have better EMI characteristics than unshielded bobbin cores. To manufacture inductors and flyback transformers/tapped inductors, an air gap is introduced by shortening the center leg of the E. Unlike a bobbin core, this configuration places the air gap in the middle of the coil, which reduces EMI.

In this work, a diode-pumped solid-state (DPSS) laser micromachining system is used to fabricate gapped E-cores from sheets of ferrite that have been thinned down to a required thickness. With refocusing, the laser can cut samples over 500$\mu$m in thickness. Fig. 6 shows several E-cores fabricated by laser micromachining as well as bobbin cores salvaged from commercial inductors. Fig. 7 illustrates the fabrication process for fully custom magnetic components. The coils are wound on temporary bobbins formed using Kapton liner and laser-cut plastic washers, and the windings are then cemented with cyanoacrylate adhesive. The temporary bobbin is removed, and two laser micromachined E-cores are inserted into the windings and glued together. This manufacturing method can yield ferrite structures with 10$\mu$m resolution and has been used to create inductors and flyback transformers/tapped inductors weighing 5-20mg.

### *B. Other components and circuit assembly methods*

The circuit substrate can account for a significant percentage of the weight in milligram-scale devices. Although flexibility is not a requirement in this application, flexible circuits manufactured by applying conventional circuit lithography to copper-laminated polymer films (e.g. DuPont Pyralux) can produce circuit substrates weighing as little as 5mg/cm$^2$.

Unlike many passive components, semiconductor packaging overhead frequently exceeds 90% of total weight. Consequently, it is highly desirable to use bare die or chip-scale packaging instead of conventionally packaged components. Chip-scale components are robust and offer the convenience of reflow soldering, but the range of components available in chip-scale packages can be limited, particularly for high-voltage devices. Bare-die components present an alternative to

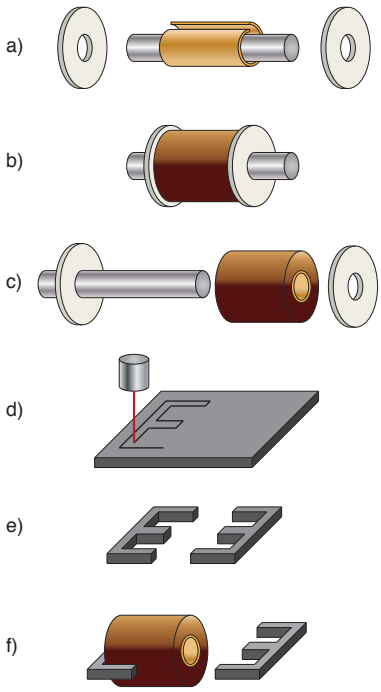


Fig. 7. Fabrication of custom magnetic components: a) temporary bobbin formation using Kapton liner and laser-cut plastic discs, b) coil winding, c) temporary bobbin removal, d) laser micromachining of ferrite core, e) core release, f) component assembly.

chip-scale packaging and can be wire-bonded directly to the circuit substrate, but some form of encapsulation is usually required to protect the fragile bond wires. When bare-die versions are not available commercially, it is possible to obtain functional bare dies from packaged devices by acid decapsulation [16].

Fig. 8 shows a range of components that can be used to implement some of the circuits of Fig. 5, including near chip-scale and bare die components, commercial and custom passive components, and a flexible substrate. Fig. 9 details the substrate fabrication and circuit assembly process for an ultralight power electronics package. In this work, circuit lithography and through-hole machining are performed using the same DPSS laser micromachining system used to fabricate custom ferrite cores.

## IV. Experimental Results

In previous work, the voltage conversion and drive circuits of Fig. 5 were implemented using discrete components on a custom flex circuit (Fig. 10). These sub-100mg circuits used custom-wound ferrite bobbin cores salvaged from commercial inductors to implement the magnetic components, resulting in poor EMI performance and difficulties in attaining good magnetic coupling. The circuits also used semiconductor components in SOT23 and SOT363 packages, which presented an opportunity for weight reduction by moving to bare-die or chip-scale components. In this paper, the tapped inductor boost converter, which serves as the DC-DC conversion stage in the circuit of Fig. 5(a), is selected as a representative topology to illustrate the techniques described in Section III, including the laser micromachining of custom magnetic components and the integration of chip-scale semiconductors and lightweight passive components on a flex substrate.

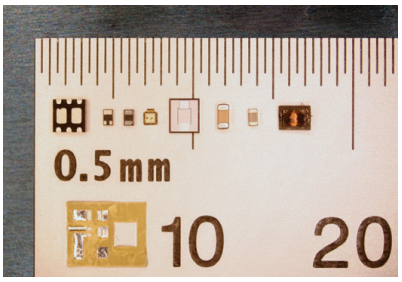


Fig. 8. Chip-scale, bare-die, and passive components used in ultralight high-voltage power circuits. Left to right: Dual 190V nFETs, 30V nFET, 325V diode, bare-die 240V nFET (decapsulated with sulfuric acid), bare-die 60V nFET (commercially available), 0.1$\mu$F 200V capacitor, 4.2$\mu$F 6.3V capacitor, 5mg laser micromachined inductor. Bottom: Flex circuit substrate manufactured from DuPont Pyralux laminate.

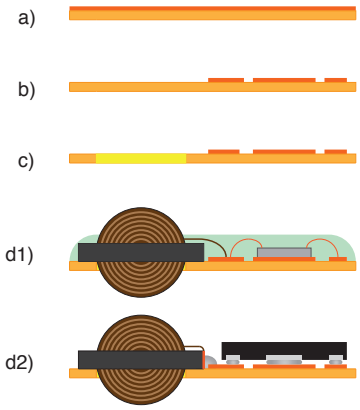


Fig. 9. Substrate fabrication and circuit assembly process: a) copper-laminated polymer substrate, b) flex circuit lithography, c) laser micromachining of through-holes, and d1) placement, bonding, and polymer encapsulation of bare-die components, or d2) placement and reflow soldering of chip-scale components.

### A. Evaluation of magnetic components

In order to gauge the performance of laser micromachined magnetic components, two versions of the tapped inductor boost converter are implemented (Fig. 11). The first version uses a custom-wound ferrite bobbin core salvaged from the Coilcraft LPS3015 series of power inductors. The second version uses a gapped E-core fabricated by laser micromachining using 8040 ferrite material from TSC Ferrite International. All other circuit parameters and components are kept the same: input capacitance ($C_{in}$ in Fig. 5) at 4.2$\mu$F, output capacitance ($C_{hv}$ in in Fig. 5) at 0.22$\mu$F, BAW101S 300V diode and ZXMN6A07F 60V nFET switch from Zetex. The

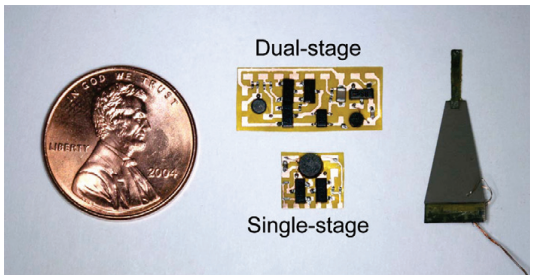


Fig. 10. Implementations of piezoelectric drive circuits next to piezoelectric bimorph actuator [5].

converters were designed with a maximum power output of 200mW at 200V and assumed an input voltage of 3.7V, the standard single-cell voltage of lithium polymer batteries. The lightweight flex circuit board is fabricated using conventional circuit lithography on a DuPont Pyralux copper-laminated polyimide film. The weight of both converters is 40mg without accounting for control functionality. In its final form, the control functionality will be implemented in a low-power custom integrated circuit, which is expected to have minimal effect on the weight and overall efficiency of the converter.

To perform a high-level optimization of the converter, a series of MATLAB scripts is used to model various loss mechanisms as a function of circuit design parameters in the expected region of operation. This approach is taken instead of SPICE simulations to reduce the computational intensity of optimizing the converter across a large number of variables, which include not only circuit design parameters such as peak inductor current and winding ratio, but also inductor core geometries, wire gauges of the primary and secondary windings, and core material properties. The losses can be broadly categorized as conduction losses, which include the switch on-state resistances, the diode forward voltage drop, and the series resistance of magnetic components; switching losses, which include the energy required to charge the gate and output capacitances of the switches, switch turn-on and turn-off losses, and diode recovery losses; and finally, magnetic losses, which include hysteresis losses, eddy current losses, and leakage inductance. The modeling of these loss mechanisms is described in more detail in [17].

A Newtons4th PSM1700 frequency response analyzer with impedance measurement attachment is used to measure inductance, parasitic resistance, and leakage inductance. Relevant parameters for both magnetic devices are given in Table II. The two magnetic components have a similar primary inductance and turns ratio. In the case of the bobbin core inductor, the MATLAB optimization procedure varies the number of turns, winding ratio, and wire gauges of the primary and secondary winding. In the case of the laser micromachined inductor, the optimization also considers the core geometry (specifically, the width, length, and height of the air gap, and the width and length of the window) and the material properties of the available ferrites. Because the gapped E-core device allows additional degrees of control over inductance by varying the core geometry, it is possible to achieve a higher inductance in

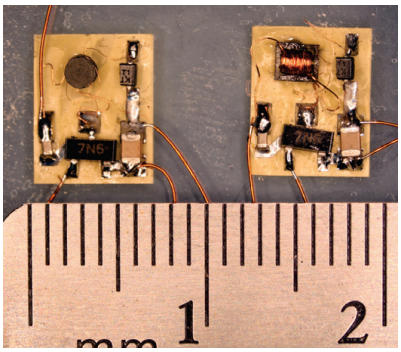


Fig. 11. Implementations of the tapped inductor boost converter using bobbin core (left) and laser micromachined core (right). All other circuit components are kept the same.

TABLE II
TAPPED INDUCTOR COMPARISON

| | Bobbin core | Gapped E-core |
|---|---|---|
| Mass | 15mg | 15mg |
| Turns ratio | 6.9 | 6.8 |
| Primary inductance | 6.20$\mu$H | 6.63$\mu$H |
| Secondary inductance | 300$\mu$H | 309$\mu$H |
| Primary resistance | 1$\Omega$ | 0.75$\Omega$ |
| Secondary resistance | 42.7$\Omega$ | 44.3$\Omega$ |
| Coupling coefficient | 0.92 | 0.95 |

a core of the same weight as compared to the bobbin core. In this case, the optimization procedure produces a gapped E-core tapped inductor with a slightly higher primary inductance and a lower primary resistance than the bobbin core. The E-core device also exhibits a higher coupling coefficient.

Fig. 12 shows the measured efficiency at different levels of output power for the two converters when configured for 150V and 200V output. Although the E-core based converter is projected to have a higher efficiency than the bobbin based converter due to a higher coupling coefficient and more optimal inductance and resistance parameters, measurements indicate that the two converters have similar efficiency, with the E-core converter exhibiting slightly higher efficiency in

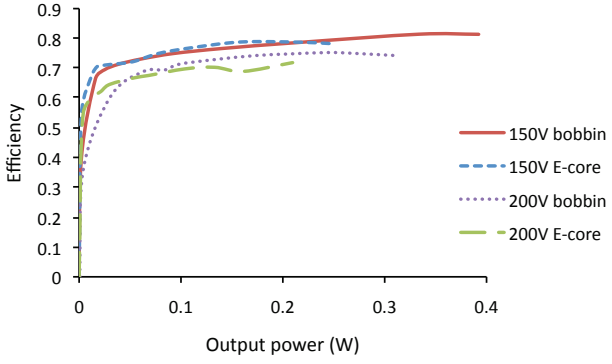


Fig. 12. Efficiency vs. output power of tapped inductor boost converters using bobbin core and laser micromachined E-core.

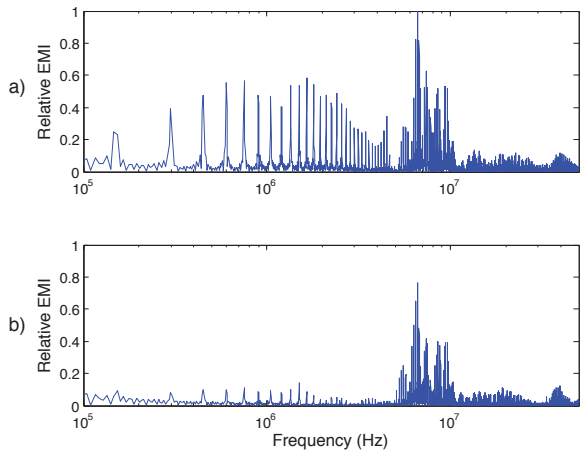


Fig. 13. Relative EMI spectra measured 1cm from bobbin core (a) and E-core (b).

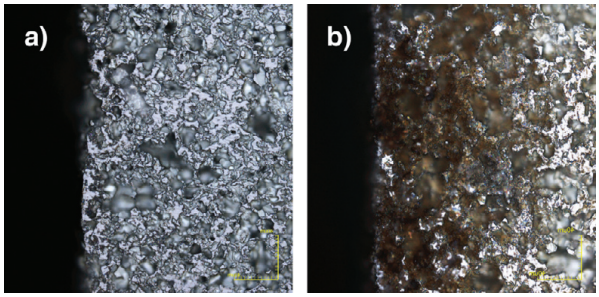


Fig. 14. Top view of ferrite edge manufactured using traditional sintering processes (a) and laser micromachining (b) under identical lighting conditions at 50X magnification (scale bars 40$\mu$m).

some regions of operation and slightly lower efficiency in others. The maximum power output of the E-core converter is 210mW at 200V and 250mW at 150V, resulting in maximum power densities of 5.25-6.25kW/kg. The maximum power output of the bobbin converter is 310mW at 200V and 390mW at 150V, resulting in power densities of 7.75-9.75kW/kg. Note that, although both converters are designed using the same optimization algorithm for a maximum power output of 200mW at 200V, lack of control over the bobbin core geometry produces a converter with a higher maximum power output.

Fig. 13 shows the relative EMI measurements obtained by placing an unshielded coil 1cm away from the bobbin and E-core magnetic devices in the same position and orientation, similar to the method of [18]. Both converters are switching at 150kHz during the measurement. This result illustrates the shielding advantage of an E-core, which significantly reduces EMI at the switching frequency and its harmonics.

Although laser micromachined magnetics allow more precise tuning of inductance, higher coupling coefficients, and reduced EMI, the measured efficiency of the converter based on these components is, on average, 5-10% lower than expected. This effect appears to be caused by a change in ferrite

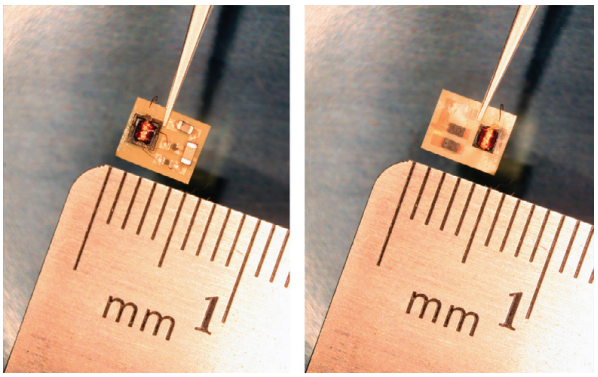


Fig. 15. Front and back view of 20mg tapped inductor boost converter.

material properties – and consequently increased magnetic losses – due to heating during the laser micromachining process. Fig. 14 shows the top view of a ferrite edge produced with conventional sintering processes as compared to an edge produced by laser micromachining. Both images are obtained under identical lighting at 50X magnification. In addition to significant discoloration, the laser micromachined sample also exhibits different porosity and surface texture, even at distances of 200-500$\mu$m away from the cut line. Further investigation is needed to verify the change in material properties and quantify its effect on magnetic losses.

### *B. Ultralight voltage converter*

To demonstrate the weight reduction potential of laser micromachined magnetics and ultralight circuit assembly methods, a tapped inductor boost converter weighing 20mg and occupying an area less than 0.25cm$^2$ (not accounting for control functionality) is implemented (Fig. 15). The converter uses an 8mg laser micromachined tapped inductor with a primary inductance of 3.1$\mu$H, winding ratio of 8.1, and coupling coefficient of 0.84. To reduce the weight of the circuit further, the DMN32D2LFB4 30V nFET switch and the BAS521LP 325V diode from Zetex are used (these are also shown in Fig. 8). The input capacitance is 4.2$\mu$F, and the output capacitance is 0.1$\mu$F.

Fig. 16 shows the measured efficiency vs. output power for the 20mg converter at 100V, 150V, and 200V output. The maximum power output is 68mW at 200V, 82.5mW at 150V, and 100mW at 100V, resulting in power densities of 3.4-5.0kW/kg. The efficiency of the converter is lower than the efficiency of the circuits in Fig. 11 due to increased losses in the transformer (the smaller size places additional constraints on inductance and resistance, and the coupling coefficient is lower as a result of manufacturing imperfections) and the switch (the DMN32D2LFB4 switch has a higher on-resistance and longer rise and fall times compared to the heavier ZXMN6A07F switch used in the circuits of Fig. 11). The efficiency of the converter can be improved by continued advances in transformer fabrication and selecting alternative bare-die or chip-scale components with more favorable parameters.

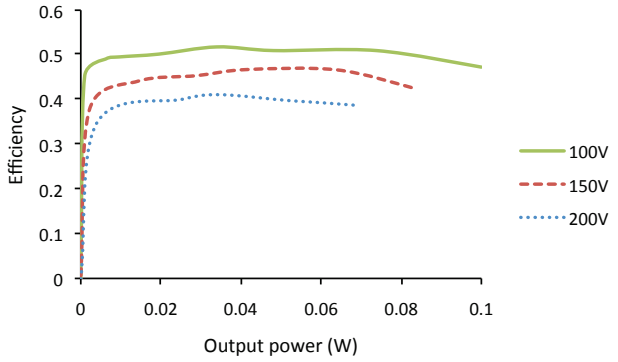


Fig. 16. Efficiency vs. output power of 20mg tapped inductor boost converter at three output voltage levels.

## V. Summary and Future Work

This paper discusses the design and fabrication of ultralight high-voltage power circuits suitable for driving piezoelectric actuators in flapping-wing robotic insects and other microrobotic applications. Piezoelectric actuator drive methods and circuit topologies are described, and techniques for implementing these topologies at minimal weight are presented, including the fabrication of custom magnetic components by laser micromachining. Comparative experimental results are presented for DC-DC converters using different types of lightweight magnetics. The techniques described in the paper culminate in the experimental realization of a converter weighing 20mg (not including control functionality) and capable of up to 70mW output at 200V and up to 100mW at 100V.

Future work will focus on continued improvement of the custom magnetics manufacturing process (including the characterization of ferrite material degradation from laser micromachining and the exploration of alternative machining methods) and fabrication of ultralight piezoelectric drive circuits suitable for flight testing on a flapping-wing robotic insect.

## Acknowledgements

The authors gratefully acknowledge support from the Wyss Institute for Biologically Inspired Engineering and the National Science Foundation (award number CCF-0926148). Any opinions, findings, conclusions, or recommendations expressed in this material are those of the authors and do not necessarily reflect those of the National Science Foundation.

## References

[1] R. J. Wood, "Liftoff of a 60mg flapping-wing MAV," in *IEEE/RSJ Int. Conf. on Intelligent Robots and Systems*, 2007, pp. 1889–1894.

[2] E. Steltz, M. Seeman, S. Avadhanula, and R. S. Fearing, "Power electronics design choice for piezoelectric microrobots," in *IEEE/RSJ Int. Conf. on Intelligent Robots and Systems*, 2006, pp. 1322–1328.

[3] D. Campolo, M. Sitti, and R. S. Fearing, "Efficient charge recovery method for driving piezoelectric actuators with quasi-square waves," *IEEE Trans. Ultrasonics, Ferroelectrics, and Frequency Control*, vol. 50, no. 3, pp. 237–244, March 2003.

[4] A. Wilhelm, B. W. Surgenor, and J. G. Pharoah, "Evaluation of a micro fuel cell as applied to a mobile robot," in *IEEE Int. Conf. on Mechatronics and Automation*, 2005, pp. 32–36.

[5] M. Karpelson, G.-Y. Wei, and R. J. Wood, "Milligram-scale high-voltage power electronics for piezoelectric microrobots," in *IEEE Int. Conf. on Robotics and Automation*, 2009, pp. 883–890.

[6] R. J. Wood, E. Steltz, and R. S. Fearing, "Optimal energy density piezoelectric bending actuators," *Sensors & Actuators: A. Physical*, vol. 119, no. 2, pp. 476–488, 2005.

[7] M. Guan and W.-H. Lao, "Studies on the circuit models of piezoelectric ceramics," in *Int. Conf. on Information Acquisition*, 2004, pp. 26–31.

[8] R. Sahai, S. Avadhanula, R. Groff, E. Steltz, R. Wood, and R. S. Fearing, "Towards a 3g crawling robot through the integration of microrobot technologies," in *IEEE Int. Conf. on Robotics and Automation*, 2006, pp. 296–302.

[9] N. Vazquez, L. Estrada, C. Hernandez, and E. Rodriguez, "The tapped-inductor boost converter," in *IEEE Int. Symposium on Industrial Electronics*, 2007, pp. 538–543.

[10] "Small, high-voltage boost converters," Maxim Semiconductor Application Note 1109, 2002.

[11] "Class D audio amplifier basics," International Rectifier Application Note AN-1071.

[12] H. Janocha and C. Stiebel, "New approach to a switching amplifier for piezoelectric actuators," in *Actuator 98*, 1998, pp. 189–192.

[13] K. Venkatesan, "Current mode controlled bidirectional flyback converter," in *IEEE Power Electronics Specialists Conf.*, 1989, pp. 835–842.

[14] A. C. Tam, W. P. Leung, and D. Krajnovich, "Excimer laser ablation of ferrites," *Journal of Applied Physics*, vol. 69, no. 4, pp. 2072 –2075, 1991.

[15] A. Kruusing, S. Leppavuori, A. Uusimaki, B. Petretis, and O. Makarova, "Micromachining of magnetic materials," *Sensors and Actuators A: Physical*, vol. 74, no. 1–3, pp. 45 –51, 1999.

[16] S. Murali and N. Srikanth, "Acid decapsulation of epoxy molded IC packages with copper wire bonds," *IEEE Trans. Electronics Packaging Manufacturing*, vol. 29, no. 3, pp. 179–183, 2006.

[17] A. Pressman, *Switching Power Supply Design*. McGraw-Hill Professional, 1998.

[18] G. Fengxun and M. Yanqiu, "A universal estimating and measurement method of EMI," in *Int. Symposium on Microwave, Antenna, Propagation and EMC Technologies for Wireless Communications*, 2007, pp. 1239–1242.